POLITECNICO DI TORINO
Repository ISTITUZIONALE

Ambient Seismic Noise and Microseismicity Monitoring of Periglacial Bodies: A Case Study on the Gran Sometta Rock Glacier (NW Italian Alps)

Original
Ambient Seismic Noise and Microseismicity Monitoring of Periglacial Bodies: A Case Study on the Gran Sometta Rock Glacier (NW Italian Alps) / Colombero, C., Di Toro, L., Khosro Anjom, F., Godio, A., Morra Di Cella, U.. - In: PERMAFROST AND PERIGLACIAL PROCESSES. - ISSN 1045-6740. - (2025). [10.1002/ppp.2286]

Availability:
This version is available at: 11583/3000712 since: 2025-06-05T16:20:06Z

Publisher:
John Wiley and Sons Ltd

Published
DOI:10.1002/ppp.2286

Terms of use:

This article is made available under terms and conditions as specified in the corresponding bibliographic description in the repository

Publisher copyright

(Article begins on next page)

15 November 2026

Check for updates

Permafrost and Periglacial Processes

WILEY

RESEARCH ARTICLE OPEN ACCESS

Ambient Seismic Noise and Microseismicity Monitoring of Periglacial Bodies: A Case Study on the Gran Sometta Rock Glacier (NW Italian Alps)

Chiara Colombero[1] | Lorena Di Toro[1] | Farbod Khosro Anjom[1] | Alberto Godio[1] | Umberto Morra Di Cella[2]

[1]Department of Environmental, Land and Infrastructure Engineering, Politecnico di Torino, Torino, Italy | [2]Climate Change Unit, Environmental Regional Protection Agency (ARPA) of Valle d'Aosta, Saint-Christophe, Italy

Correspondence: Chiara Colombero (chiara.colombero@polito.it)

Received: 9 January 2025 | **Revised:** 17 April 2025 | **Accepted:** 5 May 2025

Funding: This work was supported by the Next-GenerationEU (PE0000005 and ECS00000036).

Keywords: ambient seismic noise | microseismicity | passive seismic monitoring | rock glacier

ABSTRACT

Ambient seismic noise and microseismicity analyses are increasingly applied for the monitoring of landslides and natural hazards. These methodologies can offer a valuable monitoring tool also for glacial and periglacial bodies, to understand the internal processes driven by external modifications in air temperature and rainfall/snowfall regimes and to forecast possible melting-related hazards in the light of climate change adaptation. We applied the methods to an almost continuous year of data recorded by a network of four passive seismic stations deployed in the frontal portion of the Gran Sometta rock glacier (Aosta Valley, NW Italian Alps). The spectral analysis of ambient seismic noise revealed frequency peaks related to stratigraphic resonances inside the rock glacier. Although the resonance frequency related to the bedrock interface was constant over time, a second higher resonance frequency was identified as the effect of variations in the active layer thickness driven by external air temperature modifications at the daily and seasonal scales. Ambient seismic noise cross-correlation highlighted coherent shear wave velocity modifications inside the periglacial body. The microseismicity dataset extracted from the continuous ambient noise recordings was analyzed and clustered to further investigate the ongoing internal processes and gain insight into their source mechanism and location. The first cluster of events was found to be likely related to the basal movements of the rock glacier and to falls and slides of the debris material. The second cluster was possibly related to shallow ice and rock fracturing processes. The validation of the seismic results through simple models of the rock glacier physical and mechanical layering, the internal thermal regime and the surface displacements allowed for a comprehensive understanding of the rock glacier's reaction to the external conditions.

1 | Introduction

In the last decade, several case studies of long-term continuous ambient seismic noise and microseismicity monitoring have been reported at different scales for landslide characterization and monitoring, hydrogeological assessments, and fluvial seismology (e.g., [1, 2]). Although the continuous recordings of ambient seismic noise are generally used to identify and track resonance phenomena over time or to depict shear wave velocity variations inside the investigated bodies [3–5], microseismicity analyses are generally devoted to the detection, classification and source location of short duration events related to the ongoing processes [6–8].

Few studies applied ambient seismic noise analyses to the characterization and monitoring of glaciers and rock glaciers [9–11],

This is an open access article under the terms of the Creative Commons Attribution License, which permits use, distribution and reproduction in any medium, provided the original work is properly cited.

© 2025 The Author(s). *Permafrost and Periglacial Processes* published by John Wiley & Sons Ltd.

whereas the microseismicity of ice sheets and Alpine glaciers has already been studied to classify the source processes and locate potentially unstable compartments [12–15].

Similarly to landslide applications, ambient seismic noise spectral analyses and cross-correlation may indeed highlight modification in the seismic parameters within glacial and periglacial bodies related to the ongoing internal processes in connection with the external meteorological regime [16]. In addition, frictional processes at the base of glaciers and rock glaciers might generate stick–slip icequakes [17], which can be tracked over time for early warning purposes and compared with surface displacements. The spatiotemporal distribution of icefalls or rockfalls can also be monitored to identify the most active and prone-to-collapse sectors of the bodies and their seasonal reaction to external temperature and precipitation regimes [9, 13, 18]. The understanding and spatiotemporal tracking of these processes is becoming of uttermost importance in the light of climate change monitoring and adaptation to melting-related natural hazards [19].

Here, we analyze the passive seismic data acquired by a network of four seismic stations, deployed in the frontal portion of the Gran Sometta rock glacier (Valtournenche, Aosta Valley, NW Italian Alps). We focus on a year of almost continuous data recording, between 2020 and 2021, with acceptable data quality at the four stations. We borrow ambient seismic noise and microseismicity analyses customized for landslide monitoring (e.g., [17]) to gain information about the internal processes of the rock glacier and its seasonal reaction to the external temperature, rainfall, and snowfall stimuli. Ambient seismic noise spectral analysis and single-station spectral ratios are used to highlight resonance phenomena potentially linked to the stratigraphic structure of the rock glacier, with reference to thermally driven fluctuations in the thickness and physical properties of the active layer. Ambient seismic noise cross-correlation is further adopted to highlight possible shear wave velocity modifications within the periglacial body along the monitored period and support the interpretation of the seasonal variations in the spectral results. Finally, the microseismicity dataset extracted from the continuous ambient noise recordings is analyzed to identify clusters of recurrent events linked to the internal variations of the rock glacier. The comparison of the experimental results with numerical results obtained on simple models of the rock glacier physical and mechanical layering, together with the analysis of the internal thermal regime and surface displacement data, allow for a comprehensive understanding of the rock glacier's reaction to the external conditions. Passive seismic data processing techniques prove to be a valuable and effective instrument to characterize and monitor the evolution of periglacial bodies and potential melting-related natural hazards.

2 | Test Site and Monitoring Network

The Gran Sometta rock glacier is located close to the head of the Valtournenche Valley (Aosta Valley, NW Italian Alps; Figure 1a) at an elevation ranging from 2630 m, at the frontal portion, to 2770 m, close to the upper rock walls of the Gran Sometta peak, feeding the surface and body of the rock glacier with debris. Its surface appears as a chaotic debris mass with coarse heterogeneous blocks size (Figure 1b). The frontal portion of the rock glacier is divided in two main lobes, distinguishable from the prevalent debris cover in a black lobe to the W (mainly composed by green schists and prasinites) and a white lobe to the E (mainly marbles and dolomites). The rough and steep surface of both lobes is characterized by extensional longitudinal ridges in the axial portion and compressive transverse ridges and furrows in the terminal part. However, internally, the two lobes are characterized by different hydrological systems, likely driven by different permafrost and ice content [18], that seems more continuous and homogeneous inside the black lobe. The rock glacier thickness, estimated from the height of the rock glacier front, is approximately 20–30 m. Electrical resistivity tomography surveys acquired along the longitudinal sections of both lobes confirm a depth of approximately 30–40 m in the central part of the white lobe, reducing to 20 m towards the front. The black lobe shows a more homogenous and constant depth of approximately 20–30 m [19].

Since 2012, the site is periodically surveyed by unmanned aerial vehicle (UAV) photogrammetry and GNSS measurements for the evaluation of the rock glacier flow rates in the framework of climate change impacts on high-mountain environments and infrastructures, such as the ski resort of Cervinia. The front of the landform is indeed flowing on the ski run and road access to the cableway (Figure 1d), thus requiring constant maintenance. An artificial lake for hydropower generation (Goillet Lake; Figure 1c) is also present downward the rock glacier flow, posing additional concerns in the case of rapid movements or fluidification of the material. The highest flow rates were depicted on the black lobe, with a displacement of 3.8 m in the frontal sector between 2012 and 2015 occurring mostly in the summer months [19, 20].

From 2014 to 2018, temperature measurements inside a 15-m-deep borehole were also acquired daily in the frontal portion of the black lobe (Figure 1d), until the system was damaged by the repeated movements of the rock glacier. The measurements highlighted temperatures permanently below 0°C from a depth of approximately 6–14 m, whereas at the bottom of the borehole the temperature values were in the range of 0°C–0.5°C. In the near surface, strong seasonal variations were recorded over the years, with temperatures lower than 0°C–0.5°C from January to May along the whole borehole and reaching 15°C at 1 m depth from August to October of each year. At the same location, a GNSS-RTK antenna was also installed in late February 2021 (Figure 1d). An additional reference GNSS-RTK antenna was installed close to the Goillet lake dam (Figure 1c) to compute the relative displacements between the two monitoring points.

The four-station passive seismic network installed on-site in late July 2020 was aimed at continuously recording ambient seismic noise for the understanding of the ongoing internal processes in reaction to the external stimuli. A wireless seismic station was deployed in a stable area outside the rock glacier (S1 in Figure 1d) to be used as a reference stable station. Two stations were then placed in the frontal portion of the black lobe (S2 and S3 in Figure 1d) and one station was deployed on the white lobe (S4 in Figure 1d). Station S2 was located close to the borehole for temperature monitoring, active from 2014 to 2018. At the same location, the GNSS-RTK antenna was later

10991530, 0, Downloaded from https://onlinelibrary.wiley.com/doi/10.1002/ppp.2286 by Politecnico Di Torino Sist. Bibl Del Polit Di Torino, Wiley Online Library on [05/06/2025]. See the Terms and Conditions (https://onlinelibrary.wiley.com/terms-and-conditions) on Wiley Online Library for rules of use; OA articles are governed by the applicable Creative Commons License

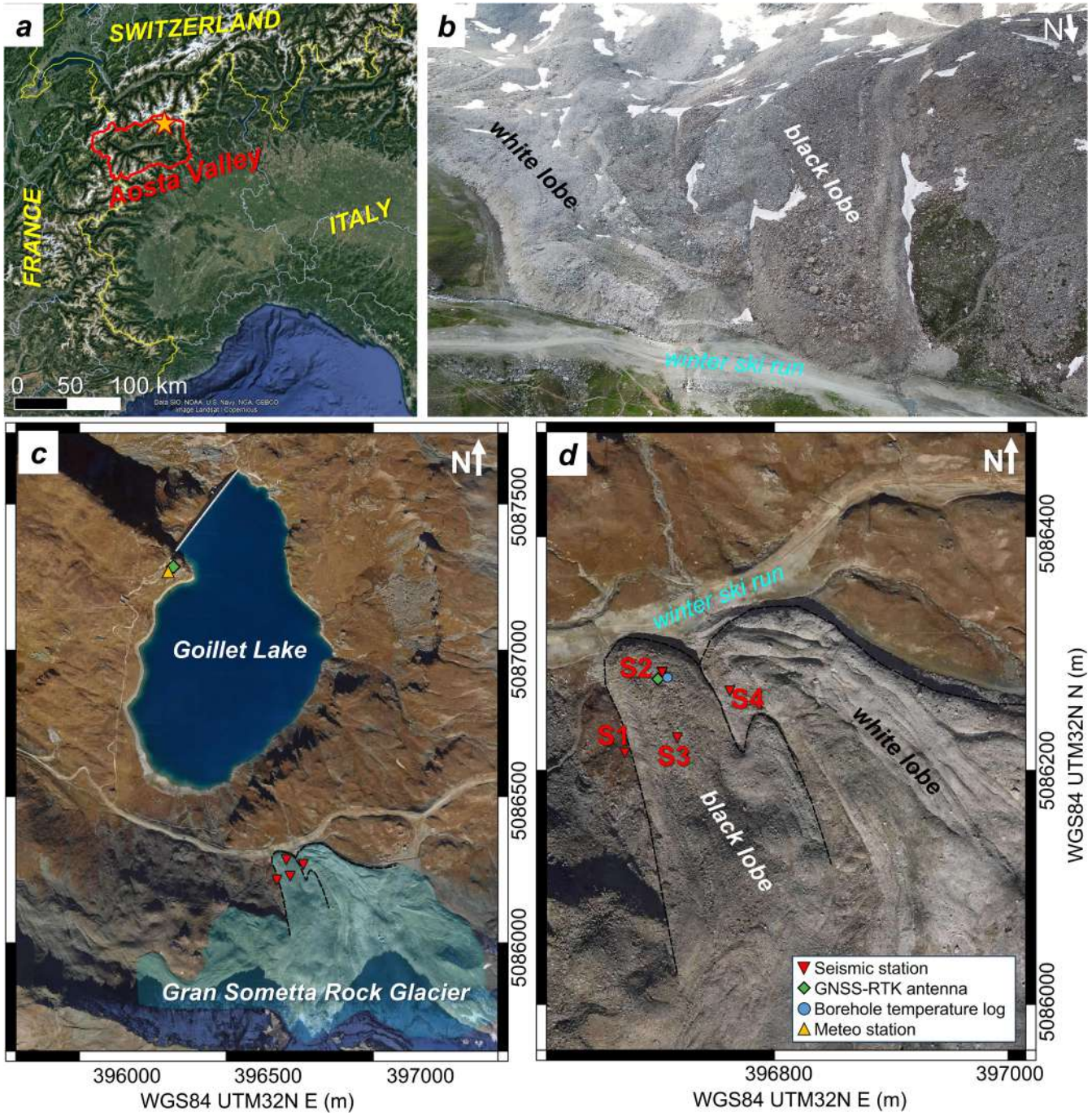


FIGURE 1 | (a) Geographic location and (b) frontal view of the Gran Sometta Rock Glacier. (c) Location of the passive seismic array and complementary temperature and surface displacement measurements, with (d) zoom on the frontal portion of the rock glacier.

installed in 2021. Each station included a 3C high-sensitivity ($200\,V\,m^{-1}\,s$) 2-Hz geophone connected to a customized digitizer/recorder (GEA–GPS, developed by PASI s.r.l. and Iridium Italia s.a.s.), ensuring continuous seismic noise recording at 250-Hz sampling frequency, low power consumption in the absence of an external power supply (approximately 30 days of autonomy), and daily remote information about the state of health of the system by a GSM–GPRS module. The synchronization between the different stations was provided by GPS timing. Data from the three components of each station were stored in 1-h files in an internal memory card. The 3C geophones were buried in the first tens of centimeters of the coarse debris cover. Due to the significant displacement rates of the frontal portion of the two lobes, the stations on the rock glacier frequently tilted during the monitored period and constant on-site network maintenance was needed. Despite this problem and the lack of power supply in some short monitoring windows, the network allowed for almost continuous data acquisition from July 2020 to October 2021 at the reference station and the ones located on the black lobe.

10991530, 0, Downloaded from https://onlinelibrary.wiley.com/doi/10.1002/ppp.2286 by Politecnico Di Torino Sist. Bibl Del Polit Di Torino, Wiley Online Library on [05/06/2025]. See the Terms and Conditions (https://onlinelibrary.wiley.com/terms-and-conditions) on Wiley Online Library for rules of use; OA articles are governed by the applicable Creative Commons License

3 | Methods

3.1 | Ambient Seismic Noise Analyses

Ambient seismic noise analyses involved the evaluation of the distribution and evolution of the noise spectral content over time at the different stations and cross-correlation of simultaneous recordings between station pairs to derive potential shear wave velocity variations inside the rock glacier.

For each monitoring point, single-station spectral ratios were computed to highlight the presence of frequency peaks in the ambient seismic noise recordings, following Valentin et al. [21] and Colombero et al. [6]. Each 1-h ambient seismic noise recording was clipped using an adaptive threshold fixed to four times the standard deviation of the whole detrended and demeaned signal to avoid the influence of episodic energetic events. Windowing in nonoverlapping segments of 100 s and tapering with a 10% cosine function were then applied. On each 100-s window, the fast Fourier transform (FFT) was then computed. The resulting amplitude spectra were then smoothed [22] and used to compute hourly average single-station H/V (horizontal to vertical) spectral ratios. The experimental H/V spectral ratios were further compared to numerical spectral ratios computed using the HV-Inv toolkit [23] for the interpretation of the experimental measurements.

Ambient seismic noise cross-correlation was computed between simultaneous 1-h recordings at station pairs. Preprocessing involved band-pass filtering (2–20 Hz), time- and frequency-domain normalization [24] of all the hourly vertical-component recordings. Hourly cross-correlograms were then computed and filtered in 5-Hz frequency bands. In each band and for each hour, the percentage of velocity change (dv/v) with respect to a reference waveform (i.e., the average of the first 360 h) was computed applying the stretching method [2, 14, 25, 26]. The cross-correlogram windows used for the stretching were selected on the coda of the 5-Hz filtered hourly cross-correlograms to avoid the direct arrivals of Rayleigh waves. The windows were therefore set to [−1.25–0.5] s and [0.5 1.25] s to keep all the coda part away from the direct arrivals but having ripples clearly distinguishable from the background noise. In detail, the negative and positive parts of each hourly cross-correlogram belonging to the stretching windows were resampled in time, to find the time shift dt/t, and consequent velocity variation dv/v, maximizing the correlation coefficient (CC) with the reference cross-correlogram of that station pair and frequency band.

3.2 | Microseismicity Analyses

A STA/LTA (short time average over long time average) algorithm was used to extract events from the continuous ambient seismic noise recordings of the four stations (STA window length = 0.2 s, LTA window length = 10 s, STA/LTA threshold for event detection = 5). The extracted events at station S2 (located on the active frontal portion of the black lobe) were classified with a K-means clustering approach based on salient time- and frequency-domain parameters of the events (i.e., ratio between the signal maximum and average amplitude A_{max}/A_{mean}, kurtosis, peak frequency in the amplitude spectrum and duration) in three main clusters (K = 3). Their temporal rate was further compared to the external air temperature, to interpret the source mechanism of each cluster, because an attempt of spatial location of the events sources was limited to the events recorded at all the stations.

The picking of first arrival times of each event at the four stations was additionally challenging due to the low S/N ratio of the events, resulting from the significant distance between the stations, their location and the general heterogeneity of the investigated media. As a consequence, a simplified approach similar to the ones described in Guillemot et al. [14], Roux et al. [10], and Lacroix and Helmstetter [27] was attempted to gain basic information on the possible source locations.

Starting from the frequency domain features of the events recorded at S2, the ambient seismic noise recordings of the four stations were band-pass filtered (2–44 Hz) and cross-correlated in a 4 s window centered around the time of the amplitude peak of each event recorded at S2, to compute time delays for the same event between all the station pairs. A weighted correlation coefficient was used to account for the different distance between station pairs in the cross-correlation results. We defined a weight $w_{i,j}$ for each couple of stations (i and j) depending on their distance $d_{i,j}$, and computed the weighted correlation coefficient as

$$CC_{w_{i,j}} = CC_{i,j} \frac{1}{1 + \left(\frac{d_{i,j}}{d_{max}}\right)^2}, \quad (1)$$

where d_{max} is the maximum interstation distance of the array (104 m between stations S1 and S4).

CC_w values of the events generally exhibited a bimodal distribution, with a highest peak in the range 0–0.2 and a second peak at around 0.5–0.7, depending on the considered station pair. We interpreted the events showing CC_w values close to 0 at one or more station pairs as not recorded by all the stations and/or inadequate for accurate delay time estimations and consequently excluded them from the source location procedure. For the delay times of the remaining 4546 events, a 2D grid search was attempted for source location, disregarding the depth dimension and only to prove the compatibility of the recorded time delays with events originating in the shallow subsurface of the rock glacier. The grid was of square size (650 m) with a node spacing of 5 m. A constant apparent velocity of the shallow subsurface was considered for the computation of the time delays expected at the four stations with event sources hypothetically centered on the grid nodes. This apparent velocity was iteratively varied from 300 to 3000 m/s with a step of 50 m/s. Finally, each event was associated with the grid node having minimum misfit with the experimental time delays.

4 | Results

4.1 | Ambient Seismic Noise Analyses

The hourly H/V ratios obtained at the four seismic stations are reported in Figure 2. Time periods with anomalous spectral content are shaded in gray and correspond to the time windows

10991530, 0, Downloaded from https://onlinelibrary.wiley.com/doi/10.1002/ppp.2286 by Politecnico Di Torino Sist. Bibl Del Polit Di Torino, Wiley Online Library on [05/06/2025]. See the Terms and Conditions (https://onlinelibrary.wiley.com/terms-and-conditions) on Wiley Online Library for rules of use; OA articles are governed by the applicable Creative Commons License

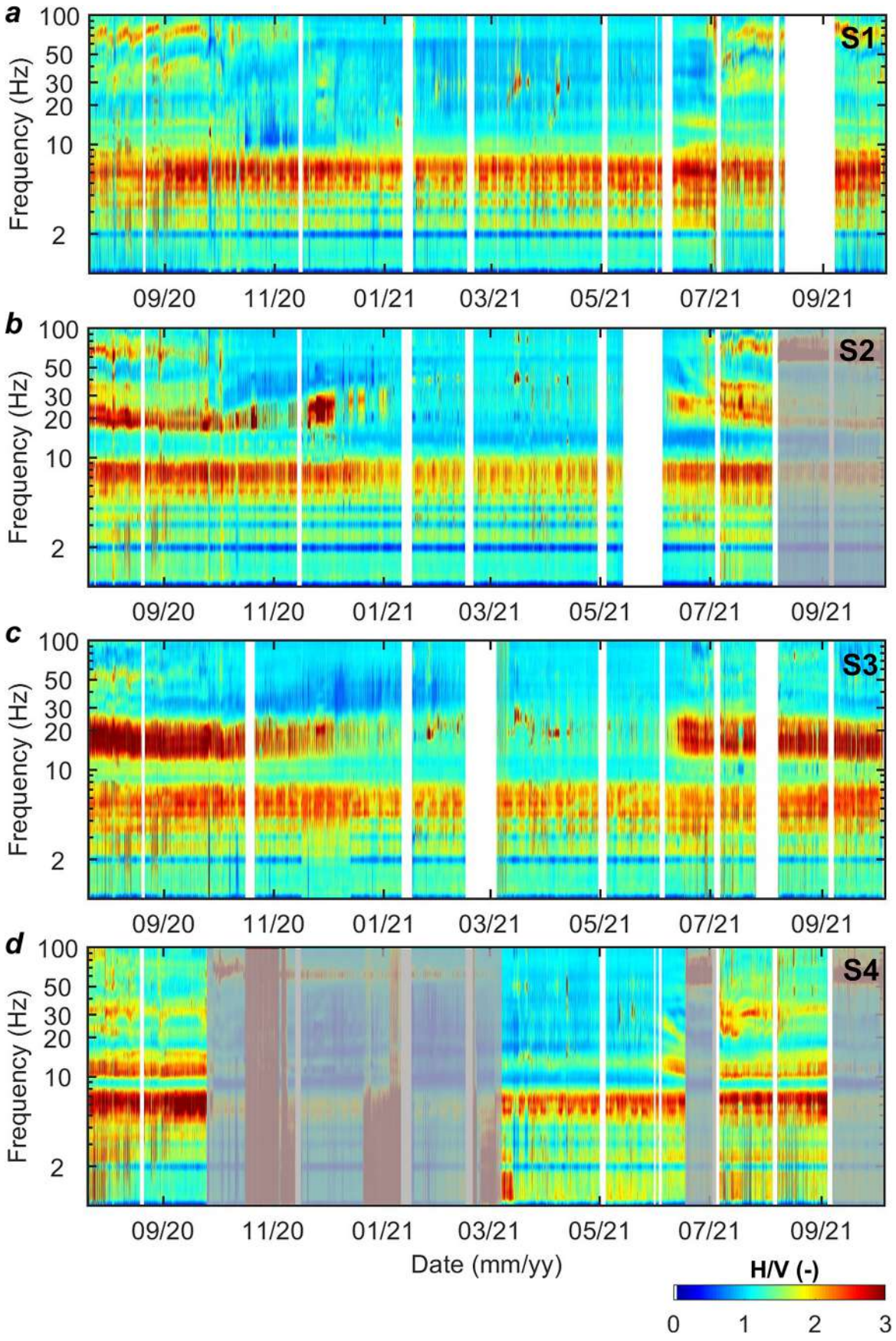


FIGURE 2 | Evolution of the hourly H/V over the monitored period at the four stations: (a) S1, (b) S2, (c) S3, and (d) S4. Shaded time windows correspond to the periods in which the stations were likely tilted; white time windows are periods with no data.

10991530, 0, Downloaded from https://onlinelibrary.wiley.com/doi/10.1002/ppp.2286 by Politecnico Di Torino Sist. Bibl Del Polit Di Torino, Wiley Online Library on [05/06/2025]. See the Terms and Conditions (https://onlinelibrary.wiley.com/terms-and-conditions) on Wiley Online Library for rules of use; OA articles are governed by the applicable Creative Commons License

in which the stations were likely tilted by the rock glacier movements.

The reference station S1 showed the best data quality over time, highlighting a predominant peak in the H/V curves centered around 6.5 Hz (Figure 2a). We interpret this peak as related to a stratigraphic resonance of the shallow deposit cover over the bedrock. In a 1D approximation, this stratigraphic resonance frequency f_0 can be written as [28]:

$$f_0 = \frac{V_s}{4h}, \quad (2)$$

where V_S and h are the shear wave velocity and thickness of the shallow deposits.

Similarly, a stable peak (f1) is found for the stations located on the rock glaciers, centered around 8 Hz for station S2 (Figure 2b), 6.5 Hz for station S3 (Figure 2c), and 6 Hz for station S4 (Figure 2d). Approximating the heterogeneous shear wave velocity of all the rock glaciers materials to 1000 m/s (following the results obtained on other rock glaciers from active seismic investigations, e.g., [14]) to roughly estimate the position of the bedrock interface; Equation (2) gives a thickness in the range from 31 m (at S2) to 38.5 m (upwards, at S3) for the black lobe, and of approximately 42 m at S4, on the white lobe. These rough estimates agree with the ERT results of Bearzot et al. [19], thus confirming the potential origin of this spectral peak.

Only minor frequency peaks are visible at S1 during the summer months at frequencies higher than 30 Hz. At the other stations, a second clear peak (f2) is found in the H/V curves. This peak starts around 20 Hz in August for the stations located on the black lobe (S2 and S3) and at approximately 12 Hz for S4. The values and spectral amplitudes of this peak are not stable over time. In fact, the f2 values tend to increase over time from October to December and decrease from June to September, but during the freezing period the peak is barely visible in few short time windows. The interpretation of this second spectral peak is further analyzed in the Discussion section as it could be linked to the meteorological data, and it could be interpreted with the support of numerical simulations on simple models of the rock glacier.

Exemplificative cross-correlation results are reported in Figure 3 between the vertical components of stations S2–S1 and S3–S1, in the 10–15 Hz frequency band, showing the highest correlation coefficients in the shear wave velocity variations estimated from the stretching method. The cross-correlation between S4 and the reference station S1 resulted in poor quality results due to the significant distance between the stations and the continuous tilting of the station located on the white lobe, as visible in Figure 2d. As a consequence, almost continuous and robust results could be achieved only on the black lobe. Despite the visible asymmetry (Figure 3a,d) likely due to the imperfect spatial distribution of noise sources around the stations, the cross-correlograms were found to be stable over time in their central portion while showing shifts in their coda. The velocity variations dv/v with respect to the average cross-correlogram of the first 360 h of recording are consequently shown in Figure 3b,e, computed on the windows [−1.25–0.5] s and [0.5 1.25] s. The strongest variations in velocity for both stations pairs are highlighted from November to May (up to +18% for S2 and +12% for S3). This velocity increase quickly drops in June to minor fluctuations in the range ±3%. The seasonal dv/v trend closely mirrors the fluctuations in the second frequency peak highlighted in the H/V spectral ratios (Figure 2).

4.2 | Microseismicity Analyses

The automatic detection of events through the STA/LTA algorithm led to several thousands of events recorded at each station (Table 1). A preliminary filtering of the detected events was therefore requested to handle a significant dataset including only the events likely related to the internal dynamics of the rock glaciers. In particular, events recorded at the four stations having duration longer than 20 s and peak frequency lower than 10 Hz were associated to local and regional earthquakes for their time- and frequency-domain behavior and time of occurrence verified in seismological catalogues. These events were therefore automatically excluded from further analysis.

In addition, the majority of the events showed high peak frequency (> 50 Hz), A_{max}/A_{mean} (> 10), and kurtosis values (> 30), but extremely short duration (< 0.4 s). These events were likely related to rainfall events and/or other transient events of anthropogenic origin. A filter based on these peak frequency, A_{max}/A_{mean}, kurtosis, and duration values were therefore applied to the dataset of detected events. The number of events detected at each station, before and after the filtering, is summarized in Table 1. After filtering, the lowest number of events was reported at the reference station S1, whereas the stations located on the black lobe detected a comparable number of events. The highest number of events occurred close to station S4, located close to the friction area between the two lobes. The number of events seems therefore to highlight a reasonable distribution, likely related to natural events.

The remaining events clustered in three main classes on the basis of their peak frequency, A_{max}/A_{mean}, kurtosis, and duration values, as shown for station S2 in Figure 4. The three clusters showed overlapping ranges of duration, kurtosis, and A_{max}/A_{mean}, and the peak frequency was consequently the main parameter allowing for discrimination between the different events. Examples of events belonging to the three clusters are shown in Figure 5.

A first cluster of events with a peak frequency consistently below 15 Hz was identified (C1 in Figure 4). The peak frequency of these events was found to be quite stable over the monitored period. The spectrograms of these events (e.g., Figure 5c) showed an almost constant energy content in the low frequency band, persisting for the whole duration of the event. We interpret these events as likely related either to rockslides or rockfalls on the surface of the rock glacier or to deeper frictional and basal sliding movements at its bottom interface.

10991530, 0, Downloaded from https://onlinelibrary.wiley.com/doi/10.1002/ppp.2286 by Politecnico Di Torino Sist. Bibl Del Polit Di Torino, Wiley Online Library on [05/06/2025]. See the Terms and Conditions (https://onlinelibrary.wiley.com/terms-and-conditions) on Wiley Online Library for rules of use; OA articles are governed by the applicable Creative Commons License

A second cluster of events (C2 in Figure 4) exhibited peak frequencies variable over time and showing one or more trends similar to ambient seismic noise results (Figures 2b and Figure 3b) from July to October. The number of these events in the freezing period (November—June) appears limited to few clusters in March—April having peak frequency of 15 and 20 Hz approximately. The spectrograms of these events (Figure 5b) showed an energy distribution over time fully comparable with micro-fracturing signatures reported in the literature (e.g., [1, 6]). The events exhibit indeed a sharp high-frequency emerging onset, followed by a sudden exponential decay of the high-frequency content. The duration of a single

TABLE 1 | Microseismic events detected through the STA/LTA algorithm and number of events after filtering the dataset on the basis of peak frequency, A_{max}/A_{mean}, kurtosis, and duration values.

Station	No. of events (*from STA/LTA*)	No. of events (*after filtering*)
S1	25,143	6978
S2	20,296	8493
S3	13,562	8677
S4	21,065	13,284

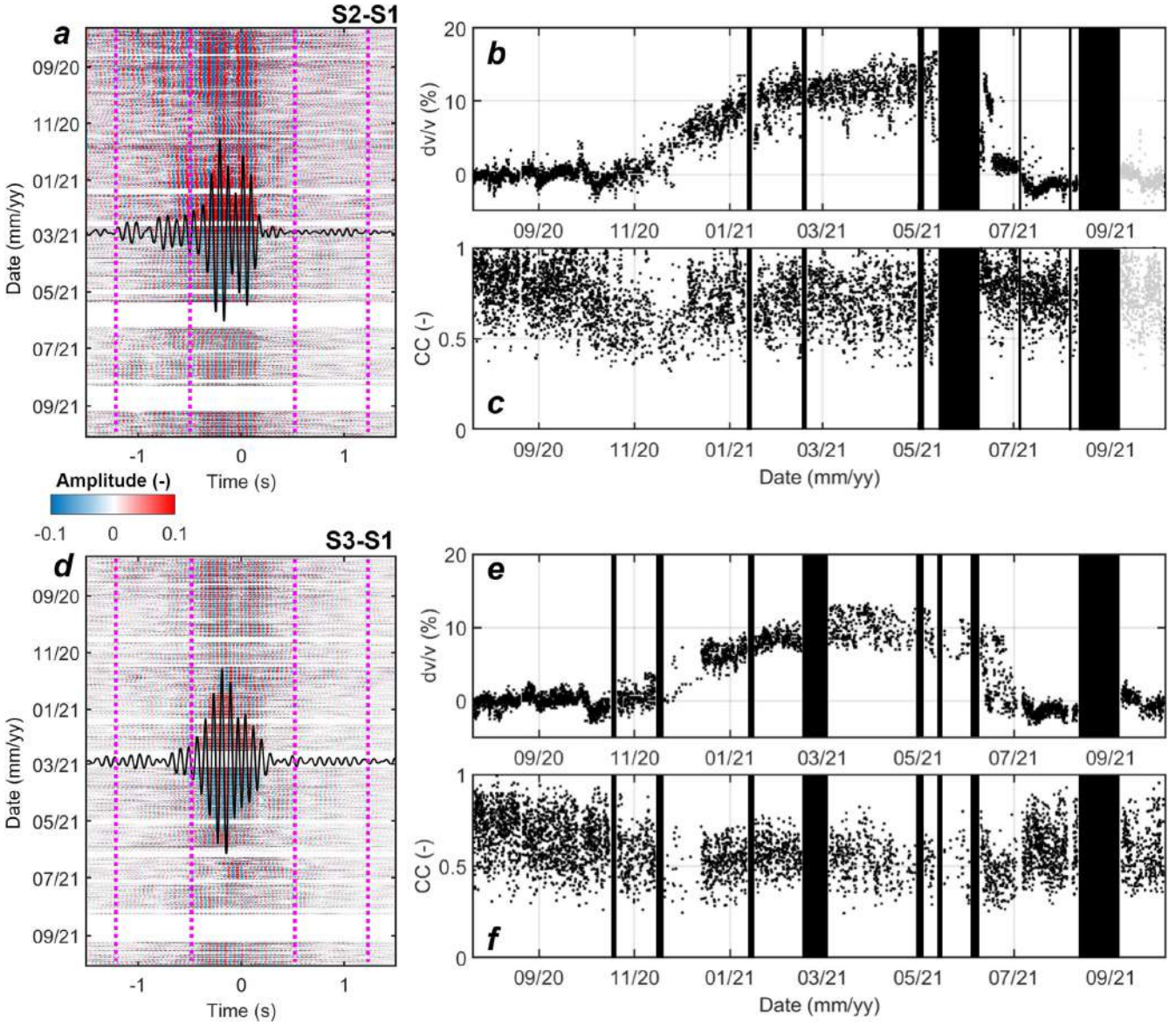


FIGURE 3 | Results of ambient seismic noise cross-correlation in the 10–15 Hz frequency band, between (a–c) S2 and S1 and (d–f) S3 and S1. (a,d) Hourly cross-correlograms between the vertical recordings of (a) S2–S1 and (d) S3–S1 in the considered time period. In (a) and (d), the reference correlograms (i.e., average of the first 360 correlograms) are displayed in the center by the continuous black line. Vertical dashed lines (in magenta) delimit the time intervals used for the stretching technique ([−1.25–0.5] s and [0.5 1.25] s). (b,e) Hourly velocity changes (dv/v) between (b) S2 and S1 and (e) S3 and S1; (c,f) related correlation coefficients. Only results having CC > 0.3 are shown. Windows with no data are marked by black boxes, windows with station tilt are shaded.

10991530, 0, Downloaded from https://onlinelibrary.wiley.com/doi/10.1002/ppp.2286 by Politecnico Di Torino Sist. Bibl Del Polit Di Torino, Wiley Online Library on [05/06/2025]. See the Terms and Conditions (https://onlinelibrary.wiley.com/terms-and-conditions) on Wiley Online Library for rules of use; OA articles are governed by the applicable Creative Commons License

event is generally short (< 1.5 s; e.g., Figure 5b), but they can occur in sequences of repeating and overlapping events, making the total event duration an ineffective parameter for classification. Given these considerations, we interpret these events as related to rock and/or ice fracturing processes (icequakes or rockquakes).

A third cluster of events (C3 in Figure 4) showed peak frequencies centered around 40 Hz. These events are almost limited to the months from January to May, because only a few events occur outside this period. Compared to the other two clusters, the distribution in peak frequency of these events is narrower, and they generally have lower kurtosis and A_{max}/A_{mean} values. The spectrograms of these events show features likely similar to the second cluster (C2) but weaker and shifted at higher frequencies. Given their temporal distribution and occurrence only in the freezing period, a possible interpretation for this cluster might be found in the passive seismic monitoring dataset acquired on another rock glacier by Guillemot et al. [14]. The authors also found increased microseismicity during the winter months, likely related to the presence of a thick snow cover at the site and explained these events as the result of snow/material compaction and stress modifications within the rock glacier due to the increased load on the surface. The possible source of these events at the monitored site is further discussed in Section 5, considering the available meteorological data for the Gran Sometta rock glacier.

Due to the low S/N ratio of the events, the heterogeneity of the investigated site, the long period of tilted recording at S4, the

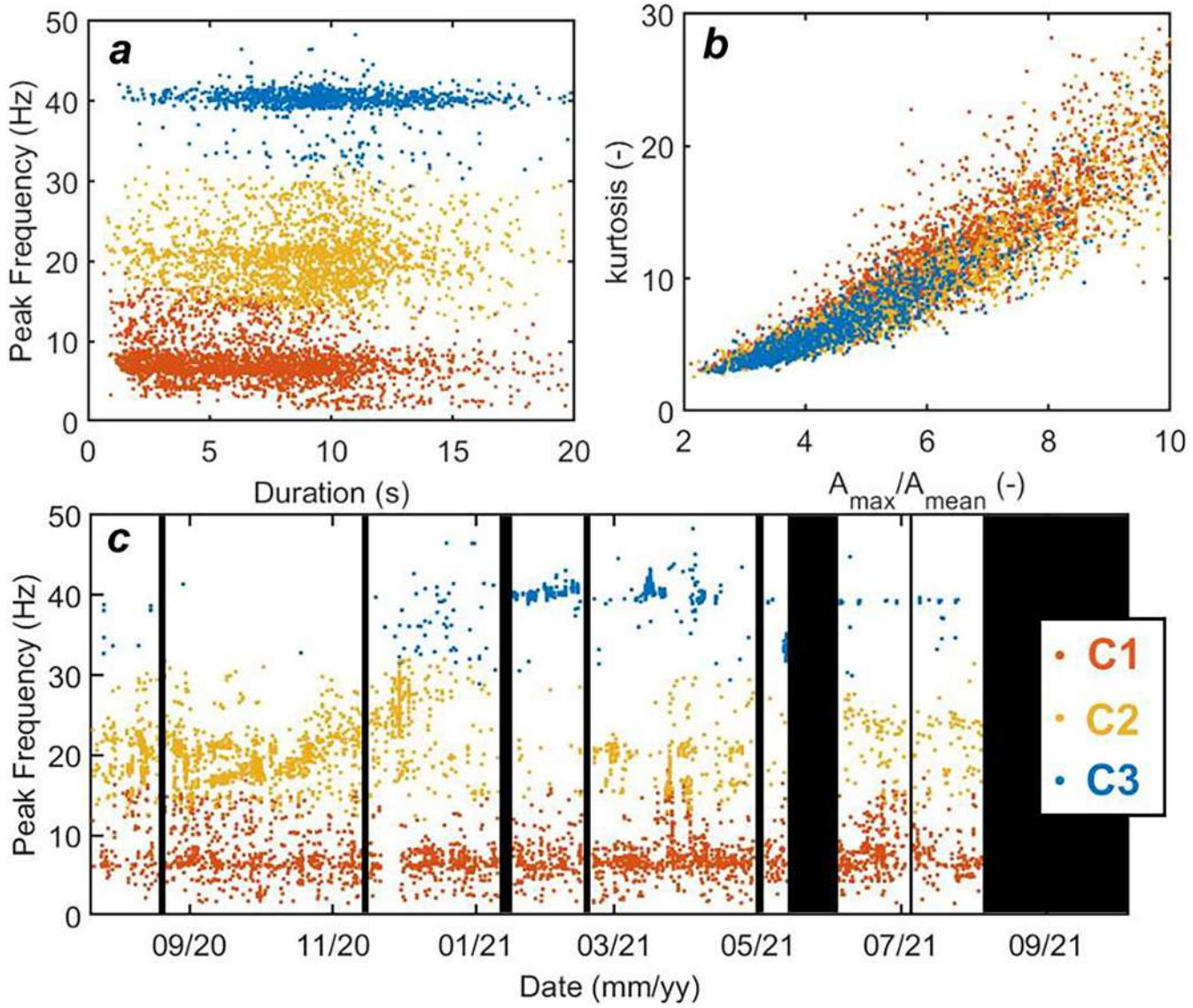


FIGURE 4 | Results of K-means clustering (K = 3) of the filtered event dataset recorded at S2. (a,b) Cross-plots of the four clustering parameters, that is, (a) duration and peak frequency of the events, (b) A_{max}/A_{mean}, and kurtosis values. (c) Temporal evolution of the peak frequency of the classified events for the whole monitored period. Black windows refer to no data periods or periods in which the station was likely tilted.

10991530, 0, Downloaded from https://onlinelibrary.wiley.com/doi/10.1002/ppp.2286 by Politecnico Di Torino Sist. Bibl Del Polit Di Torino, Wiley Online Library on [05/06/2025]. See the Terms and Conditions (https://onlinelibrary.wiley.com/terms-and-conditions) on Wiley Online Library for rules of use; OA articles are governed by the applicable Creative Commons License

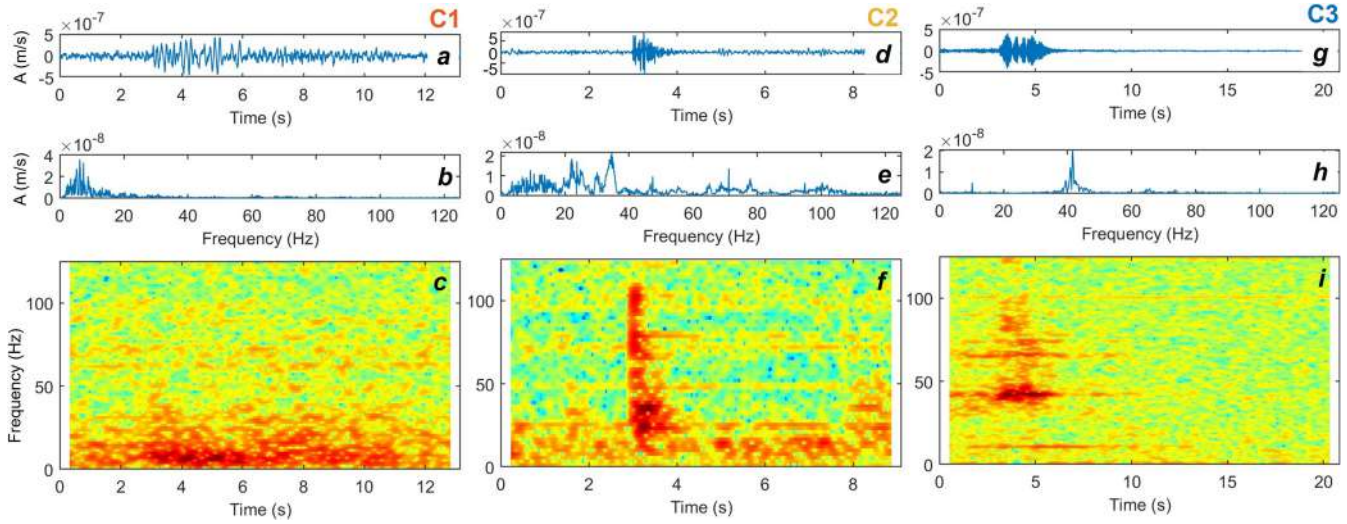


FIGURE 5 | Examples of events belonging to the three clusters of microseismicity: (a–c) C1, (d–f) C2, and (g–i) C3. Each event is shown in (a,d,g) time domain; (b,e,h) frequency domain, that is, amplitude spectrum; (c,f,i) spectrogram. Spectrograms are plotted in a color scale from blue (no energy) to red (maximum energy).

source location attempt should be regarded merely as an effort to validate the potential origin of the events from the rock glacier, rather than as a precise strategy for pinpointing their source location. The results are summarized in Figure 6, including only the 1043 events not falling at the edges of the grid after the location procedure. It should be noted that these events are only 23% of all the detected events having nonzero CC_w at all the stations pairs.

The located events fall predominantly in the frontal portion of the black lobe (Figure 6a). Considering the classification based on the K-means algorithm (Figure 6b), 569 events belong to cluster C1 (55%) and 474 events belong to cluster C2 (45%). None of the located events belong to C3, likely due to the weak and local source origin of the events of this cluster. Two areas with denser concentration of C1 sources, having constant peak frequency of approximately 5 Hz (Figure 6c), are found to the south of S3 station. These two C1 subclusters also exhibit relatively higher apparent velocities (700–800 m/s; Figure 6d), likely referring to a deeper source that might be consistent with the presence of events related to basal movements of the rock glacier inside C1. However, many other events belonging to C1 showed lower apparent velocities (400 m/s), likely referred to shallow events of rockfalls and debris movement on the rock glacier's surface.

The CC_w values of the 1043 events located in Figure 6 are summarized in Figure 7a. All these events showed CC_w values higher than 0.5. Despite the weight adopted to account for the distance between the station pairs, the station pair having the highest distance (S1–S4) resulted in generally lower values of correlation for the estimation of the arrival time delays, whereas higher correlation was generally found on the other station pairs. The residuals between the experimental time delays and the ones computed on the grid are shown in Figure 7b for the 1043 located events.

5 | Discussion

The ambient seismic noise and microseismicity results are summarized in Figure 8 in comparison with the hourly available data of the meteorological station located at the Goillet Lake, at a distance of approximately 1 km from the rock glacier's front (Figure 1c; data available at https://presidi2.regione.vda.it/str_dataview, last access on December 16 2024). The variations of the H/V peak starting at 20 Hz (f2; Figure 8c) and of the seismic shear wave velocity (Figure 8d) are clearly reversely correlated with air temperature.

The interpretation of the velocity variations is straightforward: As the air temperature falls below 0°C, all the subsurface layers progressively freeze, resulting in an increase in the shear rigidity of the materials and a progressive increase in the internal shear wave velocity. The increase in shear wave velocity at the site is higher with respect to the results of previous studies (e.g., [14]), likely due to the relatively higher frequency band considered for the computation, implying a shallower depth of investigation of the velocity changes, and differences in the landforms and environmental conditions (e.g., different elevation and thermal regime of the two areas).

The fluctuations of the frequency f2 also seem to mirror the behavior of the active layer of the rock glacier. This shallow portion of the rock glacier is indeed in direct contact with air temperature variations and its properties might be highly variable over time in reaction to the external modifications. Lower values of f2 are consequently found in the summer months, likely indicating a deeper interface between the unfrozen and frozen material within the rock glacier. At the end of the summer, with decreasing air temperature, f2 values start to increase, mirroring the decrease in depth of the unfrozen shallow layer. During winter months, f2 is weak or almost absent, corroborating the hypothesis of a completely frozen body. It appears only in short time

10991530, 0, Downloaded from https://onlinelibrary.wiley.com/doi/10.1002/ppp.2286 by Politecnico Di Torino Sist. Bibl Del Polit Di Torino, Wiley Online Library on [05/06/2025]. See the Terms and Conditions (https://onlinelibrary.wiley.com/terms-and-conditions) on Wiley Online Library for rules of use; OA articles are governed by the applicable Creative Commons License

windows centered around 40 Hz, after periods in which the air temperature rises above 0°C.

To confirm the interpretation of the spectral analysis, in Figure 9, the H/V results are further compared with numerical H/V curves and with the depth of the active layer retrieved from the borehole temperature measurements of 2014–2018 (location in Figure 1d). The model parameters adopted for the computation of the numerical H/V curves are summarized in Table 2.

Reference values of shear wave velocity and density for the materials of the rock glacier are taken from the literature on similar case studies (e.g., [14]). The bedrock depth was fixed to 35 m, coherently to the average estimate made through Equation (1) on the black lobe, whereas the depth of the unfrozen layer was

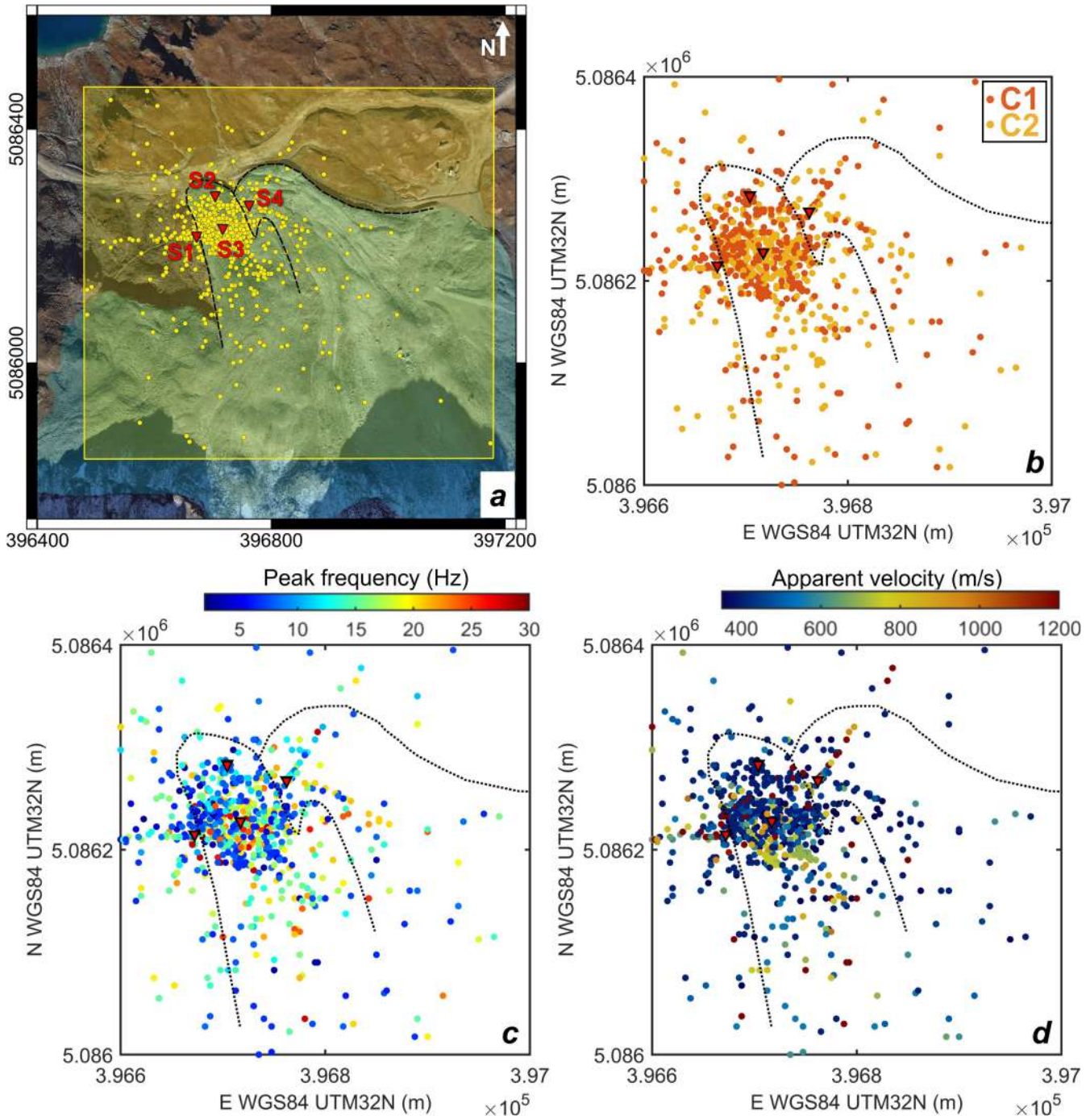


FIGURE 6 | (a) Results of source location for 1043 microseismic events falling inside the 2D grid with square size (650 m) and 5-m node spacing. The grid extent is highlighted in yellow; all the events falling at the edges of the grid are excluded from the visualization. (b) Classification of the located events from the K-means algorithm. (c) Peak frequency of the located events. (d) Apparent velocity of the grid optimizing the source location.

10991530, 0, Downloaded from https://onlinelibrary.wiley.com/doi/10.1002/ppp.2286 by Politecnico Di Torino Sist. Bibl Del Polit Di Torino, Wiley Online Library on [05/06/2025]. See the Terms and Conditions (https://onlinelibrary.wiley.com/terms-and-conditions) on Wiley Online Library for rules of use; OA articles are governed by the applicable Creative Commons License

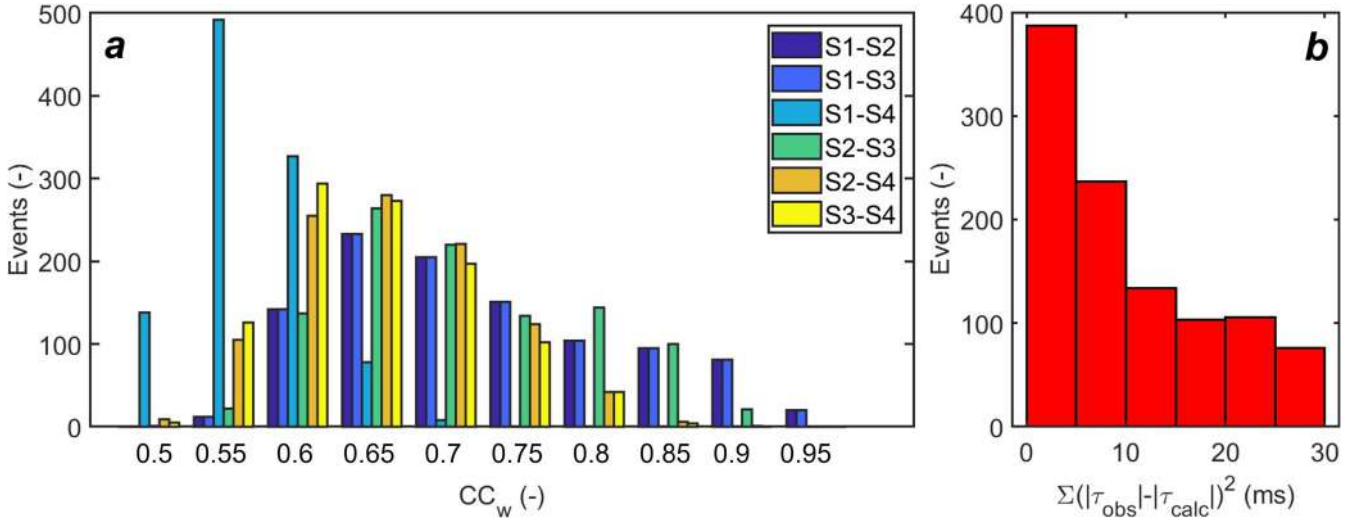


FIGURE 7 | (a) Weighted correlation coefficients (CC_w) of the time delay estimation between all station pairs for the 1043 microseismic events located inside the grid. (b) Misfit between the experimental time delays τ_{obs} of the located events and the calculated time delays τ_{calc} of the 2D grid.

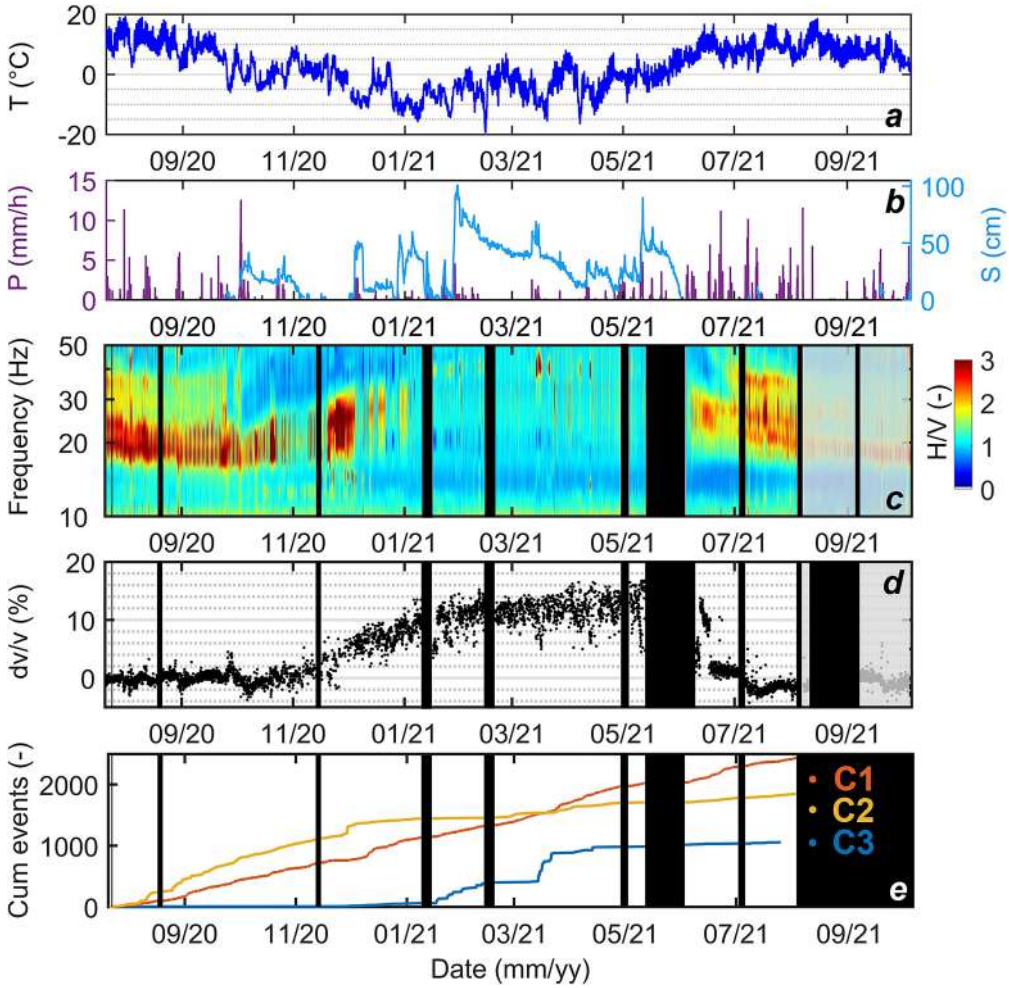


FIGURE 8 | Results of ambient seismic noise and microseismicity analysis in comparison with the meteorological data available for the site (Goillet Lake station, Aosta Valley Region): (a) hourly air temperature; (b) hourly precipitation P and snow cover height S. (c) H/V of S2 zoomed in the 10–50 Hz band. (d) Velocity variations between S2 and S1 in the 10–15 Hz frequency band. (e) Cumulative curves of the number of events belonging to the three clusters of microseismicity. Black and shaded boxes refer to periods with no data or station tilt, respectively.

10991530, 0, Downloaded from https://onlinelibrary.wiley.com/doi/10.1002/ppp.2286 by Politecnico Di Torino Sist. Bibl Del Polit Di Torino, Wiley Online Library on [05/06/2025]. See the Terms and Conditions (https://onlinelibrary.wiley.com/terms-and-conditions) on Wiley Online Library for rules of use; OA articles are governed by the applicable Creative Commons License

varied from 0 to 6 m, that is, the depth at which the borehole temperature measurements were found to be below 0°C for the whole monitored period (2014–2018).

Examples of numerical H/V curves obtained in this configuration are reported in Figure 9c. As the thickness of the unfrozen layer increases, a second peak appears in the numerical H/V curves, with spectral amplitude comparable to or higher than the first one (8 Hz approximately) related to the bedrock interface. The comparison between the numerical and the experimental curves (Figure 9d,f,h) points out a depth of the active layer close to 6 m in July, progressively thinning during the autumn and winter months (e.g., 4 m thickness at the beginning of December). In the period of January–March, the second peak is almost absent, demonstrating the complete freezing of the materials, as also validated by the deepening of the freezing interface from borehole measurements (Figure 9a). Air temperature seems therefore to be the main parameters driving the recorded seismic response at the seasonal scale. The ambient seismic noise results are further compared to the meteorological parameters in Figure 10 on a shorter time scale, outside the freezing period. A positive correlation is found between the air temperature and the f2 values at this scale, marked by a strong daily periodicity of the spectral amplitude values. This behavior marks the rapid response of the rock glacier to the external modifications in air temperature, likely linked to the high overall porosity of the materials. A similar response is found for the shear wave velocity variations. However, rainfall seems to have a higher impact on the dv/v results. The drops in dv/v occurring after the precipitation events seem only partially justified by

TABLE 2 | Model parameters adopted for the computation of the numerical H/V curves reported in Figure 9.

Layer	VS (m/s)	P (kg/m^3)	Thickness (m)
Unfrozen layer (debris + air/water)	450	1800	x = 0–6
Frozen layer (debris + ice)	1100	2000	35-x
Bedrock	2400	2700	—

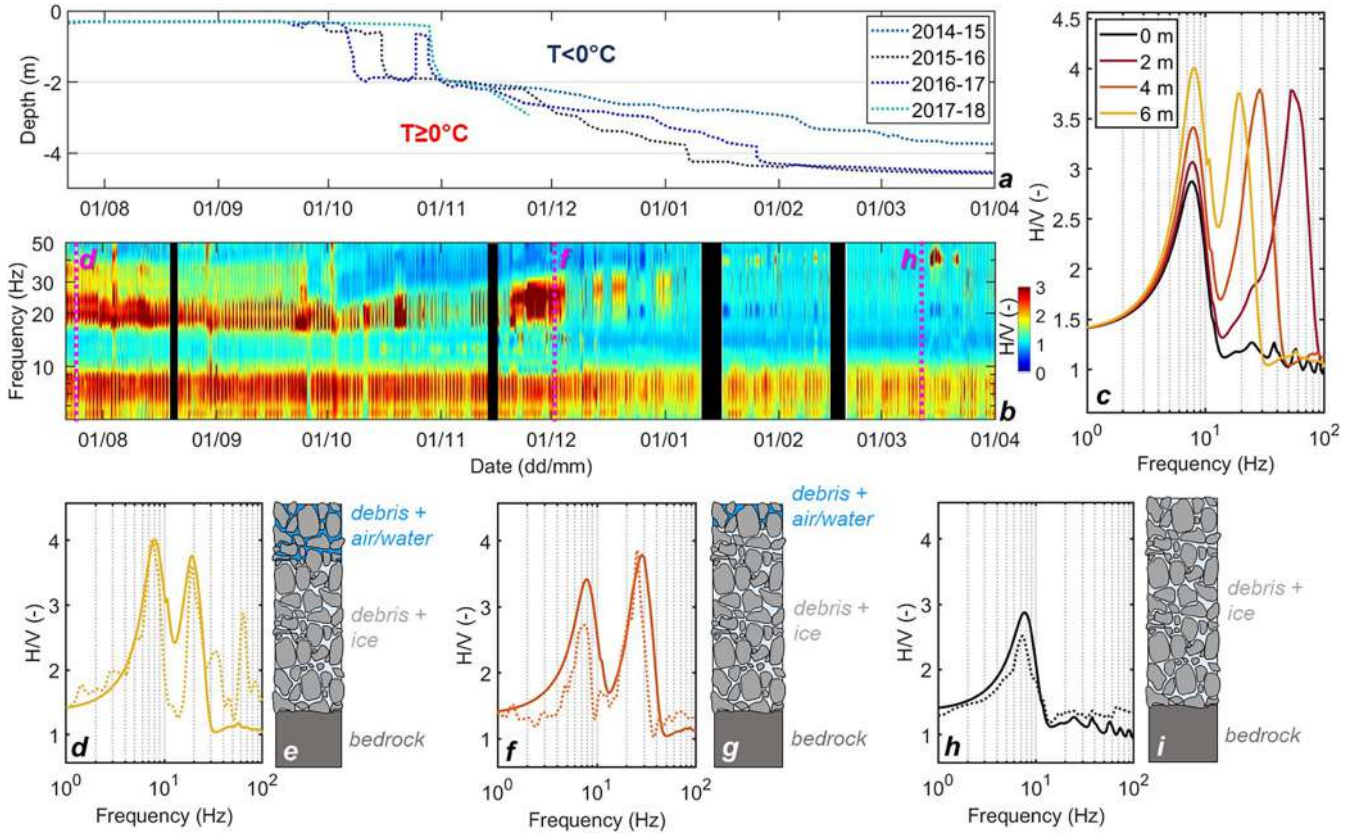


FIGURE 9 | (a) Depth of the shallow freezing interface as continuously measured in the borehole close to S2 in the months July to April of the period 2014–2018. (b) Zoom on the H/V of S2 along the same months of 2020–2021. (c) Numerical H/V spectral ratios obtained with the model parameters of Table 2. The legend refers to the thickness of the unfrozen layer. (d,f,h) Comparison between few experimental H/V curves (dashed curves, time location with magenta lines in b) and the numerical ones (solid lines, as shown in c). (e,g,i) Interpretation of the results (of d, f, and h) showing the evolution of the internal structure of the rock glacier (progressive freezing of the active layer from summer to winter months).

10991530, 0, Downloaded from https://onlinelibrary.wiley.com/doi/10.1002/ppp.2286 by Politecnico Di Torino Sist. Bibl Del Polit Di Torino, Wiley Online Library on [05/06/2025]. See the Terms and Conditions (https://onlinelibrary.wiley.com/terms-and-conditions) on Wiley Online Library for rules of use; OA articles are governed by the applicable Creative Commons License

decreasing temperature trends. As an example, after the main precipitation event at the beginning of October, the dv/v drop persists much longer than the f2, and temperature decreases. These observations might indicate deeper modifications with respect to the ones obtained by the spectral analysis, as the cross-correlation frequency band is lower (10–15 Hz). Additionally, because the shear wave velocity decreases with a decrease in the rigidity and an increase in the density of the materials, the dv/v trend might probably indicate the effect of water accumulation/snow compaction in the empty pore space of the shallower deposits.

The microseismicity of the site exhibited three clusters of recurrent events, likely related to (i) rockfalls and rockslide of the debris material on the rock glacier's surface and/or basal movements of the rock glacier (C1), (ii) icequakes or rockquakes (C2), and (iii) freezing of the materials while a snow cover was present at the site (C3). This interpretation was primarily driven by the temporal and spectral features of the events and partially supported by the event location results. The comparison of the cumulative number of events belonging to three clusters and the meteorological data (Figure 8e) further supports the interpretation. The C1 events show an almost continuous trend over the monitored period, with small steps of increased activity following rain and snow precipitation events. By contrast, the cumulative curve of C2 shows two different trends. The slope of the curve is higher in the non-freezing period, whereas it becomes flatter during the freezing period. The events of C3 are almost confined to the months from January to May. The steps with increased activity of this cluster well match with the rapid increase in snow cover at the reference meteorological station. Despite the interpretation previously given by Guillemot et al. [14] for the increase in microseismicity related to snow compaction and related internal stress modifications, it must be noticed however that the snow cover at the Gran Sometta rock glacier remains limited during the monitored period, reaching a maximum thickness of approximately 1 m (Figure 8b). The C3 events might therefore be likely related to freezing phenomena and volume expansion of ice as compared to the pore liquid water of the materials, boosted by the presence of an insulating snow cap [11, 13]. The few events assigned to C3 outside the freezing period are possibly erroneously attributed to the cluster by the automatic K-means classification procedure, based on their peak frequency values. To further confirm the different origin of the microseismicity related to the three clusters, histograms of their distribution in the different months of the year and hours of the day are reported in Figure 11, in comparison with the monthly average temperature (Figure 11a,c,e) and the hourly average temperature (Figure 11b,d,f) computed for the month

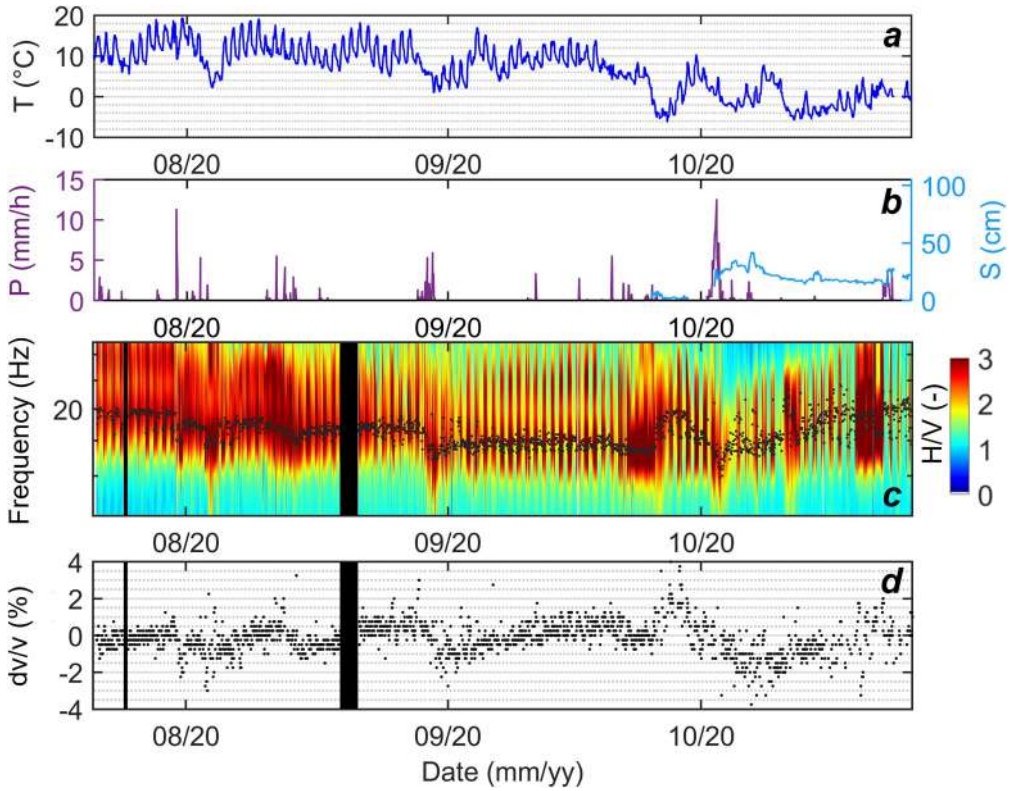


FIGURE 10 | Results of ambient seismic noise analysis zoomed over the first monitored months in comparison with the meteorological data available for the site (Goillet Lake station, Aosta Valley Region). (a) Hourly air temperature. (b) Hourly precipitation P and snow cover height S. (c) H/V of S2 zoomed in the 10–50 Hz band, with H/V peaks tracked by the black dots. (d) Velocity variations between S2 and S1 in the 10–15 Hz frequency band. Black boxes refer to periods with no data.

10991530, 0, Downloaded from https://onlinelibrary.wiley.com/doi/10.1002/ppp.2286 by Politecnico Di Torino Sist. Bibl Del Polit Di Torino, Wiley Online Library on [05/06/2025]. See the Terms and Conditions (https://onlinelibrary.wiley.com/terms-and-conditions) on Wiley Online Library for rules of use; OA articles are governed by the applicable Creative Commons License

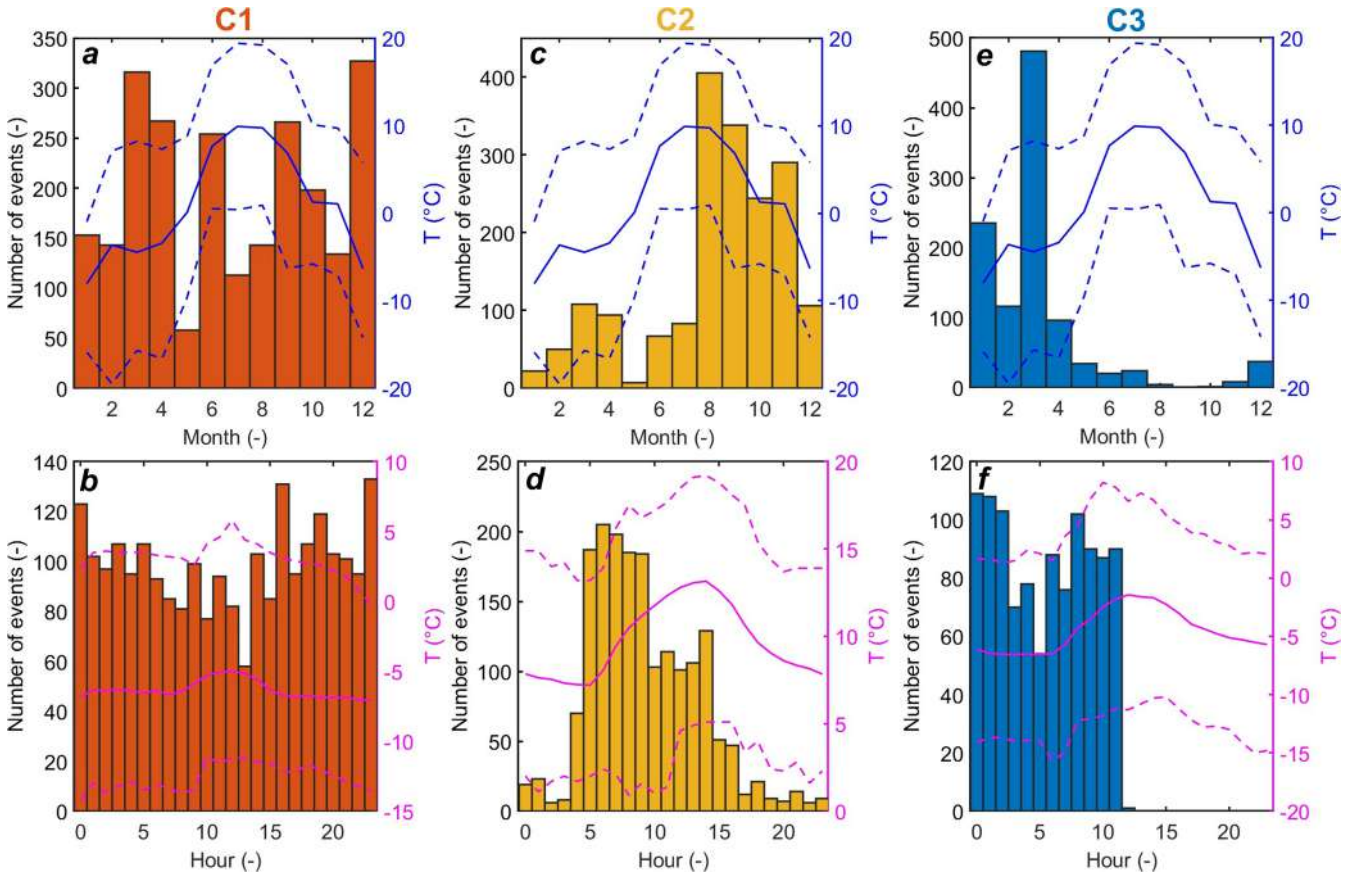


FIGURE 11 | Occurrence of the events belonging to the three clusters (a,b) C1, (c,d) C2 and (e,f) C3. (a,c,e) Monthly distribution of the events. The blue continuous line refers to the monthly average temperature; the dashed lines are the monthly minimum and maximum temperatures. (b,d,f) Hourly distribution of the events. The magenta continuous line refers to the hourly average temperature of the month having the maximum number of events (December for C1, August for C2, March for C3); the dashed lines are the related hourly minimum and maximum temperatures.

of the year having the maximum number of events related to each cluster.

C1 events are slightly more frequent in the winter months, with a peak of activity in December, followed by a similar number of events recorded in March (Figure 11a). They occur during night hours, with a peak of activity at 23:00 and 0:00 (Figure 11b). Many of these events, however, also occur in the summer months and during the afternoon-evening hours, when the air temperature decreases. As already highlighted by the apparent velocities obtained from the event location (Figure 6d), these observations might suggest the presence of different sources of microseismicity inside the cluster, which are challenging to distinguish due to their similar spectral signatures. The events occurring during winter or nighttime could be related to deeper processes, such as the basal movements of the rock glacier. In the deeper subsurface, the reaction of the rock glacier to the air temperature modifications is indeed expected to have a delay, due to the time needed by the thermal wave to trigger the basal activity. Conversely, events occurring during the summer months and/or in the afternoon hours might be linked to shallow or surface movements, such as the instability of the superficial debris cover.

The events of cluster C2 show a clearer predominant distribution in the summer months (Figure 11c), with reduced activity from December to July. They mostly occur in the morning hours, together with temperature increases (Figure 11d). This distribution might indicate a rapid thermal reaction of the shallower subsurface to the external air temperature increase, with rock and icequakes originating from the thermal expansion and fracturing of the materials.

The events related to cluster C3 have the sharpest distribution, with most events in March (Figure 11e) and occurring only in the night and morning hours of the day (Figure 11f). Their temporal distribution thus supports their interpretation as freezing related events.

The cumulative number of events related to clusters C1 and C2 in the non-freezing period of 2021 is finally compared to the planar surface displacements computed from the data of GNSS-RTK antenna deployed close to S2 in the same year (Figure 12). The displacements are steady but continuous overtime, with occasional small accelerations (e.g., June 18) preceded and followed by an increase in the activity of cluster C1.

10991530, 0, Downloaded from https://onlinelibrary.wiley.com/doi/10.1002/ppp.2286 by Politecnico Di Torino Sist. Bibl Del Polit Di Torino, Wiley Online Library on [05/06/2025]. See the Terms and Conditions (https://onlinelibrary.wiley.com/terms-and-conditions) on Wiley Online Library for rules of use; OA articles are governed by the applicable Creative Commons License

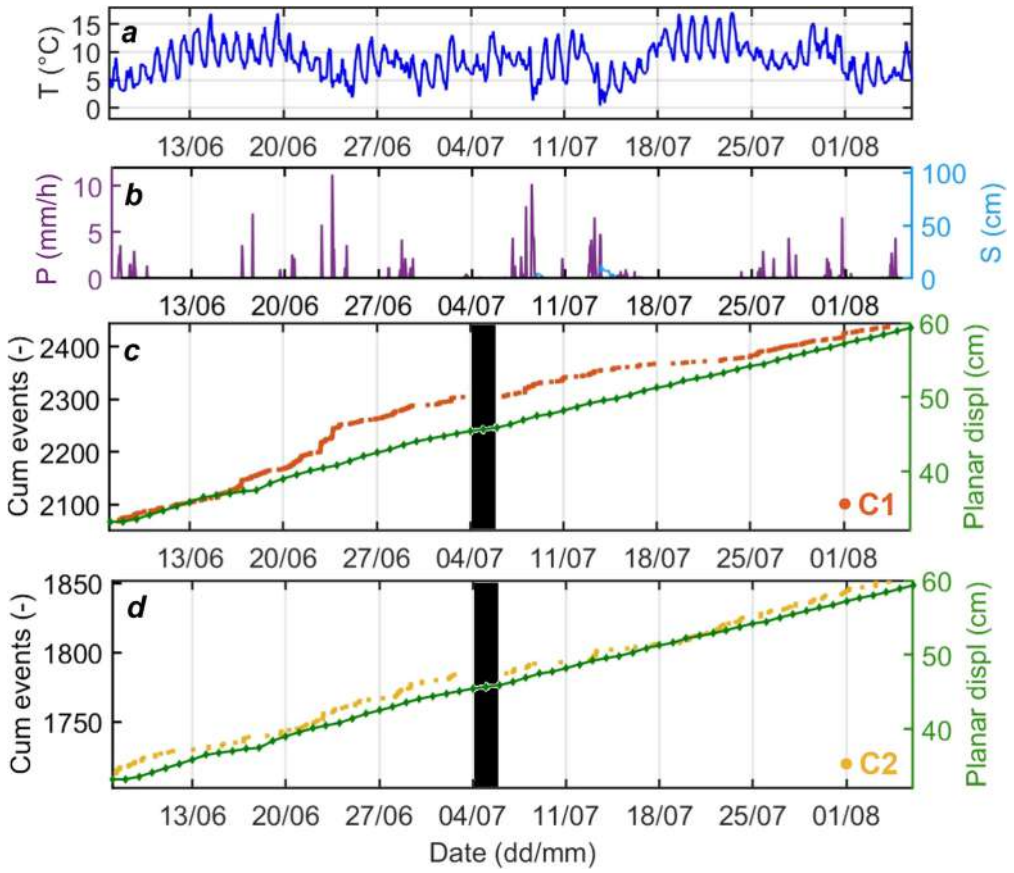


FIGURE 12 | (a) Hourly air temperature. (b) Hourly precipitation P and snow cover height S. (c,d) Cumulative number of events of the cluster C1 and C2 compared to the planar displacements retrieved from the GNSS-RTK antenna deployed close to S2.

6 | Conclusion

Ambient seismic noise and microseismicity analyses provided useful hints to analyze the internal processes of the rock glacier at both seasonal and daily scales. The results of the different processing methods agree in showing a rapid reaction of the landform to the external stimuli.

In detail, ambient seismic noise spectral analysis highlighted stratigraphic resonance phenomena related to the presence of the bedrock and to the shallow active layer of the rock glacier. The evolution of the latter can be effectively tracked over time from the passive seismic measurements in reaction to the external air temperature. Similarly, ambient noise cross-correlation interpretation strongly facilitated tracking changes in the shear wave velocity within the rock glacier in reaction to the external forcing.

The analysis of the microseismicity of the site was challenging both in terms of classification and location of the detected events. Nevertheless, the obtained results further highlight a modification in the rock glacier's response to the external conditions.

The continuous passive seismic monitoring of the rock glacier can also further guide in the identification of possible melting-related natural hazards for the site in an early warning perspective.

Acknowledgments

We warmly thank Diego Franco for his support in network installation and maintenance. We are also grateful to PASI s.r.l. and Iridium Italia s.a.s. for the development of the seismic instrumentation used for this study. We are sincerely grateful to ARPA Valle d'Aosta for the help in network deployment and maintenance and site accessibility. Data processing was carried out within the RETURN Extended Partnership and received funding from the European Union Next-GenerationEU (National Recovery and Resilience Plan—NRRP, Mission 4, Component 2, Investment 1.3–D.D. 1243 2/8/2022, PE0000005)—Vertical Spoke 2. The research activities were further supported by the project NODES which has received funding from the MUR—M4C2 1.5 of PNRR funded by the European Union—NextGenerationEU (grant agreement no. ECS00000036). Open access publishing facilitated by Politecnico di Torino, as part of the Wiley - CRUI-CARE agreement.

Conflicts of Interest

The authors declare no conflicts of interest.

Data Availability Statement

The data that support the findings of this study are available from the corresponding author upon reasonable request.

References

1. C. Colombero, A. Godio, and D. Jongmans, "Ambient Seismic Noise and Microseismicity Monitoring of a Prone-to-Fall Quartzite Tower

10991530, 0, Downloaded from https://onlinelibrary.wiley.com/doi/10.1002/ppp.2286 by Politecnico Di Torino Sist. Bibl Del Polit Di Torino, Wiley Online Library on [05/06/2025]. See the Terms and Conditions (https://onlinelibrary.wiley.com/terms-and-conditions) on Wiley Online Library for rules of use; OA articles are governed by the applicable Creative Commons License

(Ormea, NW Italy)," *Remote Sensing* 13, no. 9 (2021a): 1664, https://doi.org/10.3390/rs13091664.

2. E. Larose, S. Carrière, C. Voisin, et al., "Environmental Seismology: What Can We Learn About Earth Surface Processes With Ambient Noise?," *Journal of Applied Geophysics* 116 (2015): 62–74, https://doi.org/10.1016/j.jappgeo.2015.02.001.

3. C. Colombero, L. Baillet, C. Comina, et al., "Integration of Ambient Seismic Noise Monitoring, Displacement and Meteorological Measurements to Infer the Temperature-Controlled Long-Term Evolution of a Complex Prone-to-Fall Cliff," *Geophysical Journal International* 213, no. 3 (2018a): 1876–1897, https://doi.org/10.1093/gji/ggy090.

4. E. K. Jensen, J. R. Moore, P. R. Geimer, and R. Finnegan, "Combined Ambient Vibration and Surface Displacement Measurements for Improved Progressive Failure Monitoring at a Toppling Rock Slab in Utah, USA," *Frontiers in Earth Science* 12 (2024): 1364653, https://doi.org/10.3389/feart.2024.1364653.

5. M. Le Breton, N. Bontemps, A. Guillemot, L. Baillet, and É. Larose, "Landslide Monitoring Using Seismic Ambient Noise Correlation: Challenges and Applications," *Earth-Science Reviews* 216 (2021): 103518, https://doi.org/10.1016/j.earscirev.2021.103518.

6. C. Colombero, C. Comina, S. Vinciguerra, and P. M. Benson, "Microseismicity of an Unstable Rock Mass: From Field Monitoring to Laboratory Testing," *Journal of Geophysical Research: Solid Earth* 123, no. 2 (2018b): 1673–1693, https://doi.org/10.1002/2017JB014612.

7. A. Helmstetter and S. Garambois, "Seismic Monitoring of Séchilienne Rockslide (French Alps): Analysis of Seismic Signals and Their Correlation with Rainfalls," *Journal of Geophysical Research* 115, no. F3 (2010): F03016, https://doi.org/10.1029/2009JF001532.

8. F. Provost, C. Hibert, and J.-P. Malet, "Automatic Classification of Endogenous Landslide Seismicity Using the Random Forest Supervised Classifier," *Geophysical Research Letters* 44, no. 1 (2017): 113–120, https://doi.org/10.1002/2016GL070709.

9. A. Guillemot, A. Helmstetter, É. Larose, et al., "Seismic Monitoring in the Gugla Rock Glacier (Switzerland): Ambient Noise Correlation, Microseismicity and Modelling," *Geophysical Journal International* 221, no. 3 (2020): 1719–1735, https://doi.org/10.1093/gji/ggaa097.

10. S. Picotti, R. Francese, M. Giorgi, F. Pettenati, and J. M. Carcione, "Estimation of Glacier Thicknesses and Basal Properties Using the Horizontal-to-Vertical Component Spectral Ratio (HVSR) Technique From Passive Seismic Data," *Journal of Glaciology* 63, no. 238 (2017): 229–248, https://doi.org/10.1017/jog.2016.135.

11. E. A. Podolskiy, K. Fujita, S. Sunako, A. Tsushima, and R. B. Kayastha, "Nocturnal Thermal Fracturing of a Himalayan Debris-Covered Glacier Revealed by Ambient Seismic Noise," *Geophysical Research Letters* 45 (2018): 9699–9709, https://doi.org/10.1029/2018GL079653.

12. J. Pomeroy, A. Brisbourne, J. Evans, and D. Graham, "The Search for Seismic Signatures of Movement at the Glacier Bed in a Polythermal Valley Glacier," *Annals of Glaciology* 54, no. 64 (2013): 149–156, https://doi.org/10.3189/2013AoG64A203.

13. P.-F. Roux, D. Marsan, J.-P. Métaxian, G. O'Brien, and L. Moreau, "Microseismic Activity Within a Serac Zone in an Alpine Glacier (Glacier d'Argentière, Mont Blanc, France)," *Journal of Glaciology* 54, no. 184 (2008): 157–168, https://doi.org/10.3189/002214308784409053.

14. M. E. West, C. F. Larsen, M. Truffer, S. O'Neel, and L. LeBlanc, "Glacier Microseismicity," *Geology* 38, no. 4 (2010): 319–322, https://doi.org/10.1130/G30606.1.

15. C. G. Carr, J. D. Carmichael, E. C. Pettit, and M. Truffer, "The Influence of Environmental Microseismicity on Detection and Interpretation of Small-Magnitude Events in a Polar Glacier Setting," *Journal of Glaciology* 66, no. 259 (2020): 790–806, https://doi.org/10.1017/jog.2020.48.

16. A. Guillemot, A. Van Herwijnen, E. Larose, S. Mayer, and L. Baillet, "Effect of Snowfall on Changes in Relative Seismic Velocity Measured by Ambient Noise Correlation," *Cryosphere* 15, no. 12 (2021): 5805–5817, https://doi.org/10.5194/tc-15-5805-2021.

17. D. Gräff, M. Köpfli, B. P. Lipovsky, P. A. Selvadurai, D. Farinotti, and F. Walter, "Fine Structure of Microseismic Glacial Stick-Slip," *Geophysical Research Letters* 48, no. 22 (2021): e2021GL096043, https://doi.org/10.1029/2021GL096043.

18. A. Köhler, V. Maupin, C. Nuth, and W. van Pelt, "Characterization of Seasonal Glacial Seismicity From a Single-Station On-Ice Record at Holtedahlfonna, Svalbard," *Annals of Glaciology* 60, no. 79 (2019): 23–36, https://doi.org/10.1017/aog.2019.15.

19. R. C. Aster and J. P. Winberry, "Glacial Seismology," *Reports on Progress in Physics* 80, no. 12 (2017): 126801, https://doi.org/10.1088/1361-6633/aa8473.

20. C. Colombero, D. Jongmans, S. Fiolleau, J. Valentin, L. Baillet, and G. Bièvre, "Seismic Noise Parameters as Indicators of Reversible Modifications in Slope Stability: A Review," *Surveys in Geophysics* 42, no. 2 (2021b): 339–375, https://doi.org/10.1007/s10712-021-09632-w.

21. F. Bearzot, N. Colombo, E. Cremonese, et al., "Hydrological, Thermal, and Chemical Influence of an Intact Rock Glacier Discharge on Mountain Stream Water," *Science of the Total Environment* 876 (2023): 162777, https://doi.org/10.1016/j.scitotenv.2023.162777.

22. F. Bearzot, R. Garzonio, B. Di Mauro, et al., "Kinematics of an Alpine Rock Glacier From Multi-Temporal UAV Surveys and GNSS Data," *Geomorphology* 402 (2022): 108116, https://doi.org/10.1016/j.geomorph.2022.108116.

23. E. Dall'Asta, G. Forlani, R. Roncella, M. Santise, F. Diotri, and U. Di Morra Cella, "Unmanned Aerial Systems and DSM Matching for Rock Glacier Monitoring," *ISPRS Journal of Photogrammetry and Remote Sensing* 127 (2017): 102–114, https://doi.org/10.1016/j.isprsjprs.2016.10.003.

24. J. Valentin, A. Capron, D. Jongmans, et al., "The Dynamic Response of Prone-to-Fall Columns to Ambient Vibrations: Comparison Between Measurements and Numerical Modelling," *Geophysical Journal International* 208, no. 2 (2017): 1058–1076, https://doi.org/10.1093/gji/ggw440.

25. K. Konno and T. Ohmachi, "Ground-Motion Characteristics Estimated From Spectral Ratio Between Horizontal and Vertical Components of Microtremor," *Bulletin of the Seismological Society of America* 88, no. 1 (1998): 228–241.

26. A. García-Jerez, J. Piña-Flores, F. J. Sánchez-Sesma, F. Luzón, and M. Perton, "A Computer Code for Forward Calculation and Inversion of the H/V Spectral Ratio Under the Diffuse Field Assumption," *Computers & Geosciences* 97 (2016): 67–78, https://doi.org/10.1016/j.cageo.2016.06.016.

27. G. D. Bensen, M. H. Ritzwoller, M. P. Barmin, et al., "Processing Seismic Ambient Noise Data to Obtain Reliable Broad-Band Surface Wave Dispersion Measurements," *Geophysical Journal International* 169, no. 3 (2007): 1239–1260, https://doi.org/10.1111/j.1365-246X.2007.03374.x.

28. C. Hadziioannou, E. Larose, O. Coutant, P. Roux, and M. Campillo, "Stability of Monitoring Weak Changes in Multiply Scattering Media With Ambient Noise Correlation: Laboratory Experiments," *Journal of the Acoustical Society of America* 125 (2009): 3688–3695, https://doi.org/10.1121/1.3125345.

29. C. Sens-Schonfelder and U. Wegler, "Passive Image Interferometry and Seasonal Variations of Seismic Velocities at Merapi Volcano, Indonesia," *Geophysical Research Letters* 33 (2006): L21302, https://doi.org/10.1029/2006GL027797.

30. P. Lacroix and A. Helmstetter, "Location of Seismic Signals Associated with Microearthquakes and Rockfalls on the Sechilienne Landslide, French Alps," *Bulletin of the Seismological Society of America* 101, no. 1 (2011): 341–353, https://doi.org/10.1785/0120100110.

31. R. Dobry, I. Oweis, and A. Urzua, "Simplified Procedures for Estimating the Fundamental Period of a Soil Profile," *Bulletin of the Seismological Society of America* 66, no. 4 (1975): 1293–1324.

10991530, 0, Downloaded from https://onlinelibrary.wiley.com/doi/10.1002/ppp.2286 by Politecnico Di Torino Sist. Bibl Del Polit Di Torino, Wiley Online Library on [05/06/2025]. See the Terms and Conditions (https://onlinelibrary.wiley.com/terms-and-conditions) on Wiley Online Library for rules of use; OA articles are governed by the applicable Creative Commons License